

Globular cluster formation in the Virgo cluster

C. Corbett Moran,[★] R. Teyssier and G. Lake

Institute for Theoretical Physics, University of Zurich, Winterthurerstrasse 190, CH-8057 Zürich, Switzerland

Accepted 2014 May 28. Received 2014 May 25; in original form 2014 March 16

ABSTRACT

Metal-poor globular clusters (MPGCs) are a unique probe of the early universe, in particular the reionization era. A popular hypothesis is that the observed truncation of MPGC formation is due to reionization. Under this hypothesis, constraining the formation epoch of MPGCs provides a complementary constraint on the epoch of reionization. Moreover, as the earliest reionizing sources first formed in galaxy clusters, systems of globular clusters in galaxy clusters are of particular interest. We provide a self-consistent dark matter only zoom cosmological simulation to perform an analysis of the Virgo cluster globular cluster system by identifying the present-day globular cluster system with early, rare dark matter peaks. By analysing both the line-of-sight velocity dispersion and the surface density profile of the present-day distribution, we are able to constrain the redshift and mass of the dark matter peaks. Although found to be degenerate, we quantify a dependence on the chosen line of sight of these quantities, whose strength varies with redshift. Coupled with star formation efficiency arguments, we find a best-fitting formation mass and redshift of $\simeq 5 \times 10^8 M_\odot$ and $z \simeq 9$. We predict $\simeq 300$ intracluster MPGCs in the Virgo cluster. Our results confirm the techniques pioneered by Moore et al. when applied to the Virgo cluster and extend and justify the analytic results of Spitler et al. numerically.

Key words: methods: numerical – globular clusters: general – galaxies: clusters: individual: Virgo – galaxies: formation.

1 INTRODUCTION

Cosmic reionization of the intergalactic medium, in which its hydrogen gas changes from a neutral to an ionized state, is fundamentally intertwined with galaxy formation at high redshift. After recombination at $z \sim 1000$ (Hinshaw et al. 2013) gas in the universe was primarily neutral, but observations of the Gunn–Peterson trough in quasar spectra indicate that the universe was fully reionized by $z \sim 6$ (Gunn & Peterson 1965; Scheuer 1965). Further observations, from the evolution of the $Ly\alpha$ galaxy luminosity function (Nagamine et al. 2010) to the cosmic microwave background polarization anisotropy (Larson et al. 2011) indicate that this process was not universally instantaneous and extended from as early as $z \sim 14$ –6 (Fan, Carilli & Keating 2006). In general, ionizing sources appeared first in highly biased, dense environments (Alvarez et al. 2009).

To probe the reionization epoch, one method is to use the thousands of globular clusters (hereafter GCs) with masses from 10^4 to 10^6 solar masses which are detected in the Virgo Cluster (Peng et al. 2008) or in other nearby galaxies (Rhode, Zepf & Santos 2005) at the present day.

GC colour distribution is observed to be almost universally bimodal in colour (Zinn 1985; Gnedin 2009; Neilsen & Tsvetanov 2009), which can be ascribed principally to a metallicity difference in the two subpopulations (Brodie & Strader 2006) and references therein). This suggests two formation channels for the respective populations with a physical mechanism separating the formation of the two groups by the observed spread of ~ 1.5 Gyr. Metal-poor globular clusters (MPGCs) are of primary importance because they host the oldest stars in the whole cluster population and probe conditions at high redshift, during the earliest stages of galaxy formation (Chaboyer 1996) probing, in many formation scenarios, the period in which cosmic reionization is taking place (Rosenblatt, Faber & Blumenthal 1988; West 1993; Bromm & Clarke 2002; Côté, West & Marzke 2002). Thus, MPGCs provide what amounts to a fossil record of conditions during their formation billions of years ago.

Although the exact physical origin of GCs is still debated, it is generally admitted that GCs form in early, rare dark matter peaks (Peebles 1984; Moore et al. 2006; Boley et al. 2009). A consistent picture has emerged where MPGCs form in rare overdense fluctuations and invokes reionization to truncate their formation successfully explaining the bimodal population (Beasley et al. 2002; Santos 2003; Forbes 2006). Overdense fluctuations are the first to collapse in a cosmological context (Sheth & Tormen 1999) and thus are

[★] E-mail: corbett@physik.uzh.ch

expected to share the same spatial distribution as old stellar populations exactly such as MPGCs and halo field stars at the present day. Associating the protogalactic fragments of Searle & Zinn (1978) with the rare peaks able to cool gas in the cold dark matter (CDM) density field at $z > 10$, this indicates that MPGCs formed when the universe was less than a billion years old (Moore et al. 2006). Such a formation period is consistent with formation of the population before reionization and lends itself naturally to the hypothesis that the collapse of proto-GCs is inhibited by reionization leading to a hiatus in cluster formation (Forbes 2006). After some time in this picture, the second metal-rich population begins to form in galaxy merger events, when the gas within the host galaxies has had the chance to enrich (Brodie & Strader 2006).

Muratov & Gnedin (2010) present an alternate scenario in which MPGCs form in merger events, which at later times could produce both metal-poor and metal-rich GCs. Current measurements of cluster ages in our Galaxy can neither refute the reionization truncated scenario nor support the merger based (thus more extended in time) scenario of MPGC formation favoured by Muratov & Gnedin (2010) as these surveys cannot detect age differences below ~ 1 Gyr (De Angeli et al. 2005; Dotter et al. 2009; Marín-Franch et al. 2009). A narrow age dispersion, predicted by the reionization truncated formation scenario, remains consistent with the data (De Angeli et al. 2005; Marín-Franch et al. 2009).

In this paper, we adopt theoretical scenario in which MPGC formation is truncated by reionization focusing on a Virgo Cluster like halo allowing us to explore its consistency by comparing with M87 observational data. M87 is especially interesting theoretically as it resides in the high-density Virgo Cluster environment and hosts the most populous globular system of nearby galaxies (Côté et al. 2001), providing a rich bed of observations to compare to (Côté et al. 2001; Hanes et al. 2001). We explore the consequences of the reionization truncated formation scenario, providing hints as to the reionization epoch in a cluster environment and constraints on alternate formation scenarios.

The rare density peaks at high redshift that MPGCs form in later merge into larger objects, namely large galaxies like the Milky Way (Press & Schechter 1974; Lacey & Cole 1994). A large fraction of these galaxies ultimately end up in massive clusters of galaxies today. This three stage hierarchical process is very difficult to capture unless one uses ultrahigh resolution simulations. Such simulations give us the opportunity to explore this formation scenario by affording us the ability to trace such peaks matching them with present-day GC systems and following their kinematic and spatial distribution properties from formation until the present day.

In this paper, we are able to push our resolution capabilities to the requisite level by capturing MPGC evolution using a two stage numerical procedure. First, using ultrahigh resolution N -body simulations in the cluster region, we followed dark matter haloes down to $z \sim 4$, where the old MPGC population must be in place (Moore et al. 2006; Boley et al. 2009). We then went back to our cluster sample and used our high-redshift MPGC catalogue to mark dark matter particles as potential MPGC tracers. A halo mass cut M chosen at given redshift z corresponds to the peak overdensity ν , with higher masses at higher redshifts corresponding to more overdense, or higher ν peaks. Only particles above a requisite ν are marked. Since MPGCs are very dense and bound objects, once ν is fixed we are able to predict the MPGC population in satellite and central galaxies as well as ‘free floating’ MPGCs. An advantage of this procedure with respect to simulation physics, known hereafter as the Diemand–Moore technique, is that it is independent of the detailed baryon physics (Boley et al. 2009). By using a suite of

reference simulations at multiple resolutions, in which both higher and lower resolution simulations are able to be performed down to $z = 0$, we are able to show that this matching procedure is indeed effective and preserves the relevant physical properties we use to compare to observations, namely the GC system surface density profile and the line-of-sight velocity dispersion profile.

The Diemand–Moore technique was first shown to accurately reproduce the present-day GC system in the Galaxy (Moore et al. 2006) via an ultrahigh resolution N -body simulation. Spitler et al. (2012) use this technique to provide evidence for inhomogeneous reionization in the local universe from MPGCs. The Diemand–Moore technique was introduced to use the spatial concentration of MPGCs relative to the host galaxy’s halo mass profile to constrain the rarity of the haloes that the MPGCs formed within. This technique requires MPGC surface density profiles from observations, a halo mass model of the galaxy hosting the MPGCs and a framework to interpret the spatial bias of the MPGCs. Their fitting to the observed GC system properties of M87, NGC 1407, and our Galaxy enabled them to derive a joint constraint on z_{reion} of $10.5^{+1.0}_{-0.9}$ with individual constraints of $z_{\text{reion}} = 12.1^{+1.6}_{-1.1}$, $11.0^{+1.7}_{-1.7}$, $7.8^{+2.0}_{-1.8}$ for the Milky Way, NGC 1407 and M87, respectively. Intriguingly, they find that while the reionization process is thought to begin earliest in high-density environments, such as the Virgo Cluster in which M87 resides, it completes last in the cluster environment.

Motivated to explore and validate the assumptions behind this counterintuitive result reached by Spitler et al. (2012), we continue this line of research and explore ways to relax some of the assumptions made by Spitler et al. (2012). Specifically, we get rid of the assumption of spherical symmetry, performing the analysis numerically versus analytically, and assume molecular in addition to atomic cooling in star formation arguments used to check the consistency of our candidate redshift and mass pairs which correspond to a given density peak height, the number of standard deviations above the mean mass–density level at that epoch (Lacey & Cole 1994). Using our simulations coupled with the matching technique, we present comparisons to observed properties in M87 and show numerical improvements to the previous analytic results and constraints of Spitler et al. (2012).

In Section 2, we describe the numerical methods adopted for our simulations as well as our matching technique, and show that such resolution bridging is indeed possible preserving the relevant physics. In Section 3, we show the present-day particles corresponding to high-sigma peaks at high redshift indeed reproduce the blue globular cluster distribution at $z = 0$ in a Virgo like object by comparing to the observational properties of M87. In Section 4, we present the best-fitting model, with error bars based on line-of-sight variations, with associated discussion.

2 SIMULATIONS AND HALO MATCHING PROCEDURE

We performed three simulations of a Virgo analogue halo of successively higher resolutions: low, high, and ultrahigh of which the mass and spatial resolution is detailed in Table 1. Full details of technical parameters and simulation methodology used are given in Appendix A. Recent work by Geen, Slyz & Devriendt (2013) explores matching simulation runs with different physics by identifying haloes between the simulations. In this work, we deploy a novel matching technique to directly identify particles between simulations of different resolutions which allows us to run the ultrahigh resolution simulation only until $z \sim 4$. Using the matching

Table 1. Mass and spatial resolution for our simulations.

Name	$m_{\text{cdm}}(10^6 M_{\odot})$	$\Delta x_{\text{min}}(\text{kpc } h^{-1})$
Low	54	1.5
High	5.4	0.8
Ultrahigh	0.54	0.4

technique together with the high-resolution simulation, we are able to analyse robustly physical quantities such as the surface density and velocity dispersion profiles at $z = 0$ despite not running the ultrahigh resolution simulation to the present day. Only the low- and high-resolution simulations were run to $z = 0$ and were used to validate our matching technique.

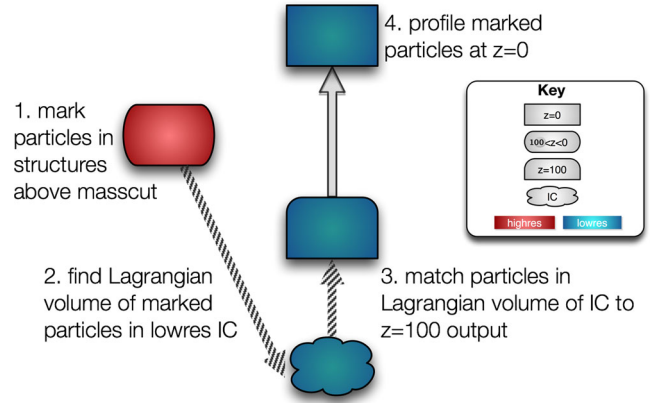
Steps in the matching procedure are detailed as follows:

(i) Run halo finder HOP (Eisenstein & Hut 1998), on the high-resolution simulation at a given redshift. This outputs a group ID associated with each particle, which is 0 if the particle is not associated with a group.

(ii) For haloes above a given mass cut and below a given contamination fraction (the fraction of mass of particles at the highest resolution relative to total mass), mark the particles within these haloes. This was done via a modified version of the `poshalo.f90` routine available in the standard `RAMSES` distribution called `markparticles.f90`. The routine `poshalo.f90` reads in the haloes computed by HOP and outputs the number of particles, contamination factor, centre and velocity of each halo. `markparticles.f90` is identical to this routine but additionally checks if a particle's assigned group's mass is above the mass cut and its group's contamination fraction is below the contamination cut. For the particles whose respective groups meet this criterion their IDs are written to an ASCII file on disc.

(iii) Trace marked particles in the high-resolution simulation at $z = 0$ to the low-resolution initial condition file at $z = 105$. This was done using the `geticmask.f90` routine available in the standard `RAMSES` distribution. This is a utility that for the purpose of zoom simulations allows the user to select a group of particles specified by their associated global particles ID in an ASCII file `partID.dat`, typically within the same halo, and trace back to their Lagrangian volume to a `GRAFIC` initial condition file. The first `RAMSES` simulation output, the particle IDs to be traced, and the `GRAFIC` initial condition files are given as input. Here, as we had `RAMSES` particle IDs, we wanted to trace back to initial conditions as an output of the previous step we could simply re-purpose the code for this, even as these particle IDs correspond to different haloes with the caveat as we wanted to mark these and only these particles, we removed the Zel'dovich approximation drifting so as to not mark drifted particles. This outputs a file called `ic_refmap` indicating those particles 'marked' in the `GRAFIC` initial condition file.

(iv) Match the low-resolution initial condition file at $z \approx 100$ to the first output of the simulation, identifying marked particles in the low-resolution simulation. This was done via the `track_particles` C++ routine developed as part of this work built upon Oliver Hahn's C++ library to access `RAMSES` snapshot files, `libRAMSES++` (Hahn 2008) and the `fio` library Potter (2007) which handles `GRAFIC` initial condition files. `track_particles` uses the C++ library to read in the `RAMSES` file checks for each particle in the `RAMSES` simulation the library reads in if the particle lies in the inner zoom simulation box, if it does it computes its grid cell in the

**Figure 1.** Steps in the matching procedure.

`GRAFIC` IC accessed using the `fio` library, goes to that grid cell in the `GRAFIC` IC, check in the `ic_refmap` if it is marked, and if so write the particle ID in the lower resolution simulation to a binary array of integers, with a header indicating the total number of particles.

(v) Compute the profile of the marked particles at $z = 0$ in the low-resolution simulation about these particles. This was done via a modified version of `cylpart2prof.f90` available as part of the standard `RAMSES` distribution called appropriately `markedcylpart2prof.f90`, which is identical except that it additionally reads in the binary file of marked particles computed in the previous step and only profiles those particles which are marked. Thus, the code takes in both a `RAMSES` output (we used that of $z = 0$) and a marked particle file in the previously specified binary format. This gives us the desired profiled quantities we are interested in: cylindrical surface density distribution and circular velocity dispersion properties, for comparison with observation.

A schematic of the matching procedure is depicted in Fig. 1.

2.1 Matching technique effectiveness

To verify the matching procedure, we used the low- and the high-resolution simulations given in Table 1, each of which we were able to run to $z = 0$. Thus, we could compare the result of the procedure above, specifically comparing the following two cylindrical surface density distribution and circular velocity dispersion properties

(a) The profiled quantities of low-resolution particles in the low-resolution simulation at $z = 0$, which were marked at high redshift in the high-resolution simulation.

(b) The profiled quantities of high-resolution particles in the high-resolution simulation at $z = 0$, which were marked at high redshift in the high-resolution simulation.

If (a) and (b) are sufficiently close, we can be convinced of the technique's effectiveness when applied to the high- and ultrahigh resolution simulations, allowing us to forgo the cost of running the ultrahigh resolution simulation to $z = 0$.

Fig. 2 shows first that the curves at subsequently higher resolution are consistent, with similar features, and in the case of density near identical slopes. Note that a lower resolution particle is about 10 times more massive than a higher resolution particle, so selecting 1000 particles at higher resolution, corresponds to selecting 100 particles at lower resolution. This shows that we can successfully mark particles at high redshift and higher resolution, and step down

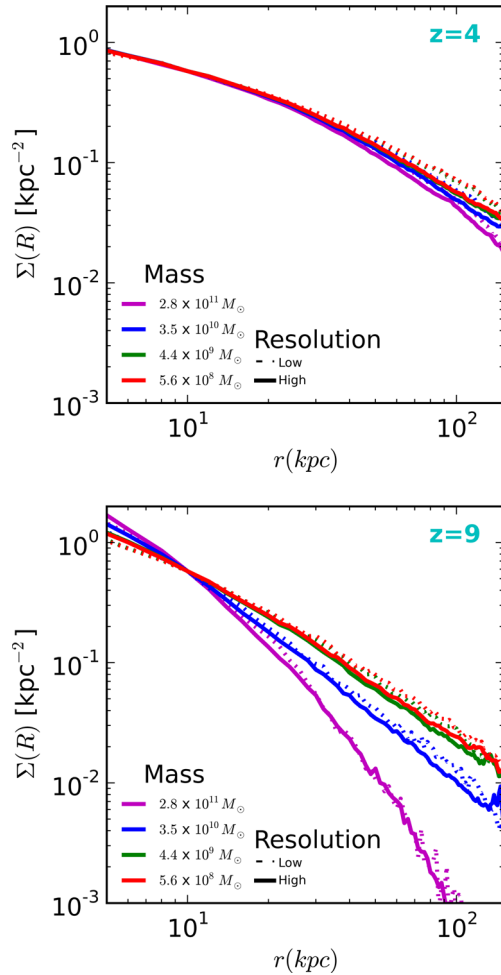


Figure 2. Showing that the matching technique between particles marked at higher resolution to particles at low resolution is suitable for recovering profile information at lower resolution.

one order of magnitude in the simulation that is run to $z = 0$ and still recover the correct profile for those marked particles at $z = 0$, with the added advantage of having a much more detailed trace of their kinematical properties (by an order of magnitude) in the high-resolution simulation at high redshift. Finally, we can see that there remains an advantage to working at the highest resolution possible, as the lower resolution profiles tend to overstate the mass, velocity, and densities, with these profiles becoming more refined at higher resolution, as would be expected.

3 RESULTS

To compare to observational data existing for M87's GC system, which exists for both cylindrical surface density distribution and line-of-sight velocity dispersion, we computed these quantities for our simulations for various formation scenarios. The scenarios that correspond best to the observational data we deem most likely. Each of these quantities has a dependence on chosen line of sight for the measurement. To quantify this dependence, for all of our analysis, we randomized over the line of sight and error bars indicate the scatter in the measured quantity over 100 such random lines of sight and the results are detailed in this section.

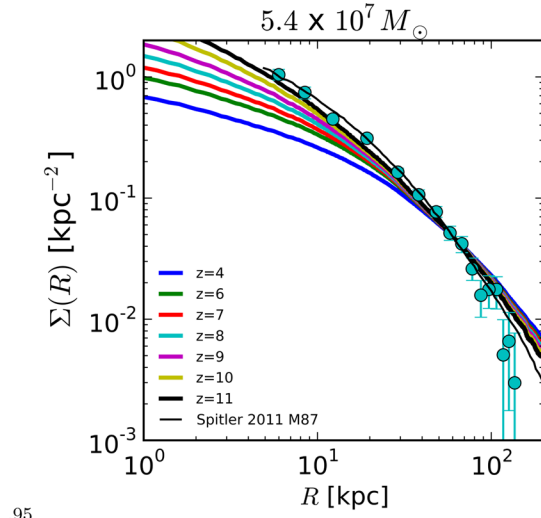
3.1 Surface density distribution and line-of-sight velocity dispersion

The variation of surface density with redshift cut for a fixed mass cut is depicted in Fig. 3 and shows that for a mass $M \simeq 5 \times 10^7 M_\odot$ the best-fitting redshift cut is $z \simeq 11$, for $M \simeq 5 \times 10^8 M_\odot$ $z \simeq 9$, for $M \simeq 5 \times 10^9 M_\odot$ $z \simeq 7$. Thus, for surface density profiles, the higher the mass cut the lower the redshift cut that is consistent with the Virgo data.

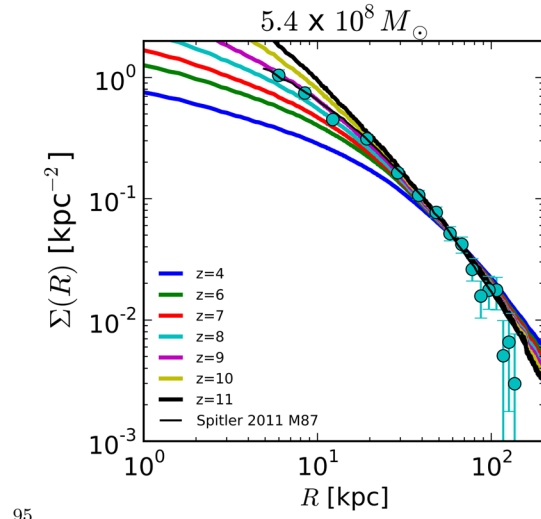
The variation of the line-of-sight velocity dispersion with redshift cut for fixed mass, as depicted in Fig. 4 shows that at $M \simeq 5 \times 10^7 M_\odot$ all redshifts are significantly too hot, with $z \simeq 11$ being the best fit. Again at $M \simeq 5 \times 10^8 M_\odot$ the best fit is $z \simeq 11$ with a degeneracy of redshifts, getting hotter as the redshift decreases but in general hovering around the same value and following the same trend. Finally, for $M \simeq 5 \times 10^9 M_\odot$, we have some discrimination between the velocity dispersions of various redshift cuts, and a good indication that $z \simeq 9$ or $z \simeq 10$ could be potential best fits.

The central region of the velocity dispersion data in the observations increases as the radius decreases while our simulation results show a sharp decrease in velocity dispersion as the radius decreases. This is probably due to the absence of a Brightest Central Galaxy (BCG) in our simulation results, which would cause the central increase in velocity dispersion seen in the observational data. Thus, comparisons between simulations and observations are done outside of the inner 20 kpc, and we do see that in the region 20–100 kpc there are several models which go through all observational data bins within the error bars. Another caveat is that our halo mass is not perfectly normalized to that of M87, meaning that the general hotter-to-colder trend in the velocity dispersion would hold, no matter the normalization, but the exact normalized value could change.

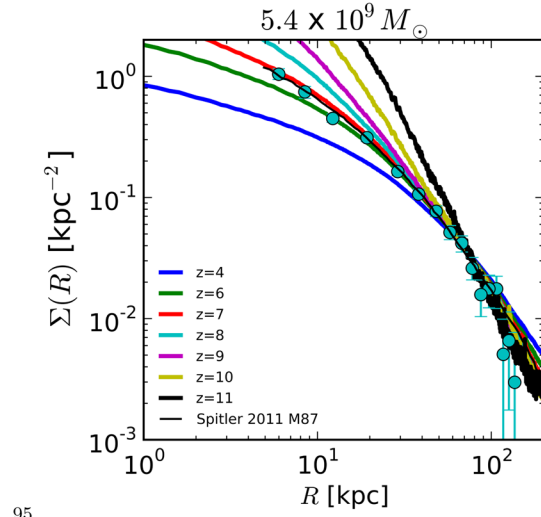
The data show a downward trend in velocity dispersion, and yet the simulations show in general an upward trend with radius. In general, higher sigma peaks produce colder distributions in the simulations and a flatter, though in general still rising, measurement of the dispersion outskirts of the halo. Diemand, Madau & Moore (2005) see a similar effect when employing the Diemand–Moore technique; with increasing peak height the globular cluster distribution becomes both colder at $z = 0$ and the velocity dispersion profile becomes shallower. Observationally, indications of a rising velocity dispersion at the edge of a galaxy when the intracluster light and halo stars are considered exist for some galaxies considered. In one of the 13 BCG galaxies considered in Fisher, Illingworth & Franx (1995), there is a stark example of a rising dispersion curve in BCG IC 1101 the dominant member of Abell 2029, previously observed to have a rising velocity dispersion in Dressler (1979). Several additional BCGs analysed in Fisher et al. (1995) show a flat velocity dispersion profile. Our results predict the GC population of M87 should show a rising velocity dispersion curve. There is not yet a published velocity dispersion profile that we are aware of for M87 beyond ~ 120 kpc, but such data should offer confirmation to our analysis and provide an additional self-consistent way to break the minimum mass/minimum redshift degeneracy in peak height of formation sites of GCs in M87. Recent results by Murphy, Gebhardt & Cradit (2014) show a hint of confirming our predictions, measuring a rising GC velocity dispersion in M87 out to 45 kpc, and additional observational data beyond this will provide important constraints to our theoretical picture.



.95



.95



.95

Figure 3. Variation of surface density at $z = 0$ of the globular cluster population with redshift cut for a fixed mass cut. Cyan points, with associated error bars, are observational data for M87 MPGCs (Strader et al. 2011).

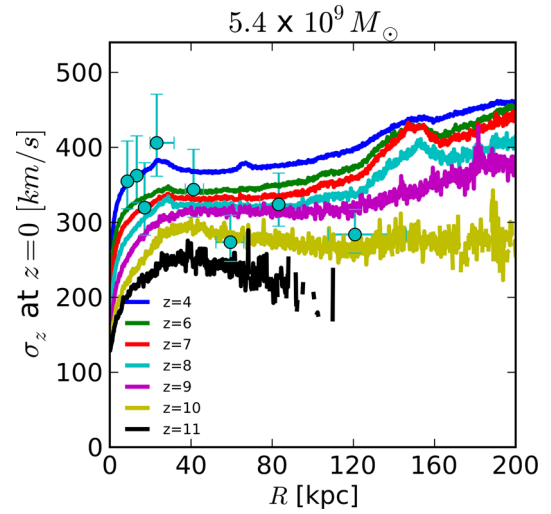
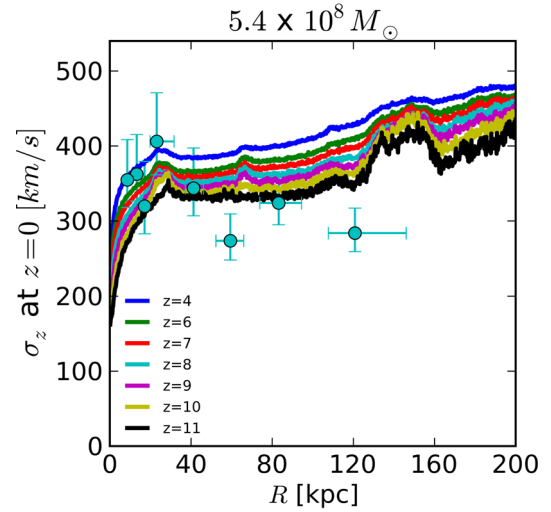
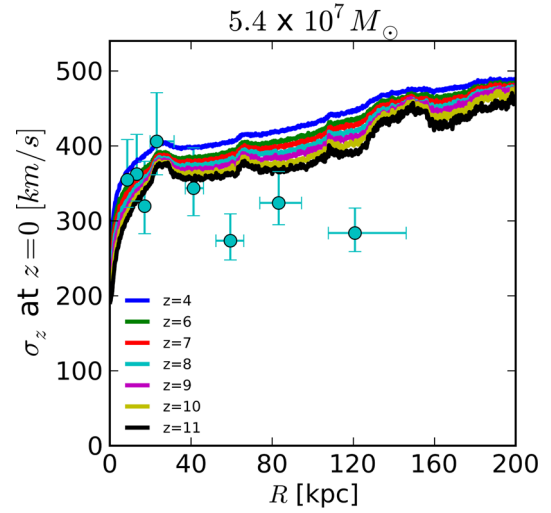


Figure 4. Variation of the line-of-sight velocity dispersion with redshift cut for a fixed mass cut. Cyan points, with associated error bars, are observational data for M87 MPGCs (Strader et al. 2011).

3.1.1 Velocity dispersion

We examine the anisotropy of the velocity distribution theoretically and numerically to test the Diemand analytical approach and to examine whether we can glean information from the velocity distribution additional to that given by the surface density profile.

The anisotropy parameter β is defined as

$$\beta = 1 - \frac{1}{2} \frac{\sigma_t^2}{\sigma_r^2} \quad (1)$$

and discriminates between radial and tangentially biased orbits. As orbits approach perfectly radial, $\beta \rightarrow 1$, whereas $\beta < 0$ means the orbits are tangentially biased. By way of example perfectly circular orbits are completely tangentially biased i.e. $\beta \rightarrow -\infty$. β is in general determined by the dependence of the distribution function on the total angular momentum (Binney & Tremaine 2011).

In terms of β the Jeans equation for a spherical system is

$$\frac{d(v\bar{v}_r^2)}{dr} + 2\frac{\beta}{r}v\bar{v}_r^2 = -v\frac{d\Phi}{dr}, \quad (2)$$

where v is the density of the population, \bar{v} the mean velocity.

Considering $\bar{v}_r^2 \propto \sigma_z^2$ and $v \propto r^{-\alpha}$ we can rewrite the Jeans equation as

$$-\frac{\alpha}{r}\sigma_z^2 + \frac{d}{dr}\sigma_z^2 + \frac{2\beta}{r}\sigma_z^2 = -\frac{d\Phi}{dr} \quad (3)$$

Assuming $\frac{d}{dr}\sigma_z^2$ is negligible, we solve for σ_z^2 :

$$\sigma_z^2 = \frac{r}{\alpha - 2\beta} \left(\frac{d\Phi}{dr} \right). \quad (4)$$

As a sanity check of the validity of this approximation we must verify $\alpha \geq 2\beta$. In the inner part, we expect this to easily hold as $\beta < 1$ and $\alpha \simeq 2$. In the outermost parts of the halo, β may approach 1, but in this regime $\alpha > 2$ generally. Moreover, we expect in this regime the approximation $\frac{d}{dr}\sigma_z^2$ as negligible to break down, as σ_z^2 will be sharply decreasing, and to in turn allow for a range of α values in the analysis.

Performing an analysis of β on our halo, subtracting out the halo bulk velocity, we see that material originating in higher sigma peaks is more radially biased at $z = 0$ as depicted in Fig. 6. As in Sparre & Hansen (2012), we see a radial bias in β as a whole.

Material derived from a higher sigma peaks has a higher β parameter as seen in Fig. 5, for such material from equation (4), we expect the velocity dispersion to be in general lower. This is exactly the behaviour we see in Fig. 9, where for higher z or higher mass, corresponding to material originating in higher sigma peaks, there is systematically a lower σ_z with the effects being most prominent at the highest sigma level analysed (e.g. $z \simeq 11$, $m = 5.4 \times 10^9 M_\odot$).

For two haloes undergoing a merger, the centrally concentrated populations – exactly those originating from high-sigma peaks – behave more like point particles than two populations of more extended objects undergoing a merger. We expect that after undergoing the merger, the concentrated populations maintain more of the memory of the merger event than the extended population, in which case the result is in effect smoothed. If the β value is thus a function of an initial impact parameter b of a merger event, we would expect β to be a stronger function of b for centrally concentrated material than for the general population with the more centrally concentrated the material the stronger the effect. We see this clearly in Fig. 6, where material originating in high-sigma peaks follows the same trend as the general population simply exaggerated in effect the magnitude of the exaggeration increasing with increasing sigma. In this manner β encodes information about past major mergers.

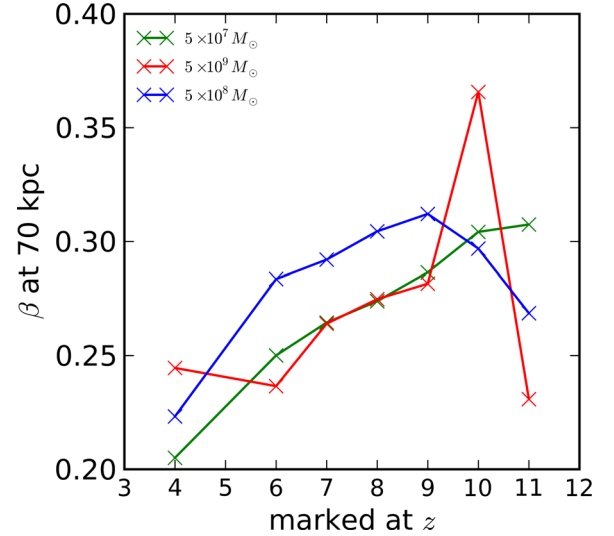


Figure 5. β as measured at 70 kpc.

A few caveats to our results. First, results in the literature generally smooth over hundreds of haloes. Sparre & Hansen (2012) quote a β of 0.4 for cluster sized haloes independent of radius which was computed by averaging the effects of particular substructure or merger events through this process. We are dealing with a single halo, and so these effects are not averaged out. Secondly, Sparre & Hansen (2012) show that β is a simplistic analysis for non-spherical systems, as clusters such as in our analysis in general are, and propose a β dependent on velocity dispersions along and perpendicular to the halo major axis. We thus consider our results as more of an indication of a trend than a proof of one.

Côté et al. (2001) found that the MPGCs of M87 had a slight tangential bias of $\beta = -0.4$. We see this behaviour as well simply at a larger radius with β dipping below zero outside of 200 kpc before settling around 0 at the virial radius. This result concretely shows different dynamical behaviour of the MPGC subpopulation as we predict. The difference in our prediction amounts only to a difference in our merger history as simulated versus the merger history as experienced by M87. While our simulation is an M87 analogue, it is naturally just one realization and its history is not demanded to be identical. The observations of Côté et al. (2001) provide an important clue that our model of MPGC formation results in correct dynamical behaviour at $z = 0$, the radius of the tangential bias onset difference explained by the differences in merger histories of our simulated halo versus that of M87.

3.2 Star formation efficiency

As a consistency check, we compare the mass we must produce in stars of GCs at a given mass and redshift cut (corresponding to a peak rarity ν) to the mass that could have come from star formation at the marked redshift. Using a virial radius of $R \simeq 1 \text{ Mpc}$ (Urban et al. 2011) and the mass model for Virgo from McLaughlin (1999), we get a virial mass M_{200} for Virgo of $\simeq 2\text{--}3 \times 10^{14} M_\odot$. We note that our simulated cluster has a lower mass of $\simeq 1 \times 10^{14} M_\odot$.

To estimate the present-day blue globular cluster (hereafter BGC) population mass in Virgo, we use the fits computed in Côté et al. (2001) to the BGC population. Noting that the data extend to only 100 kpc, we compute a lower and upper bound to the present-day BGC population mass by extending our integration to 100 kpc and $\simeq 1 \text{ Mpc}$. The integrated BGC mass we find are $\simeq 3 \times 10^9$ and

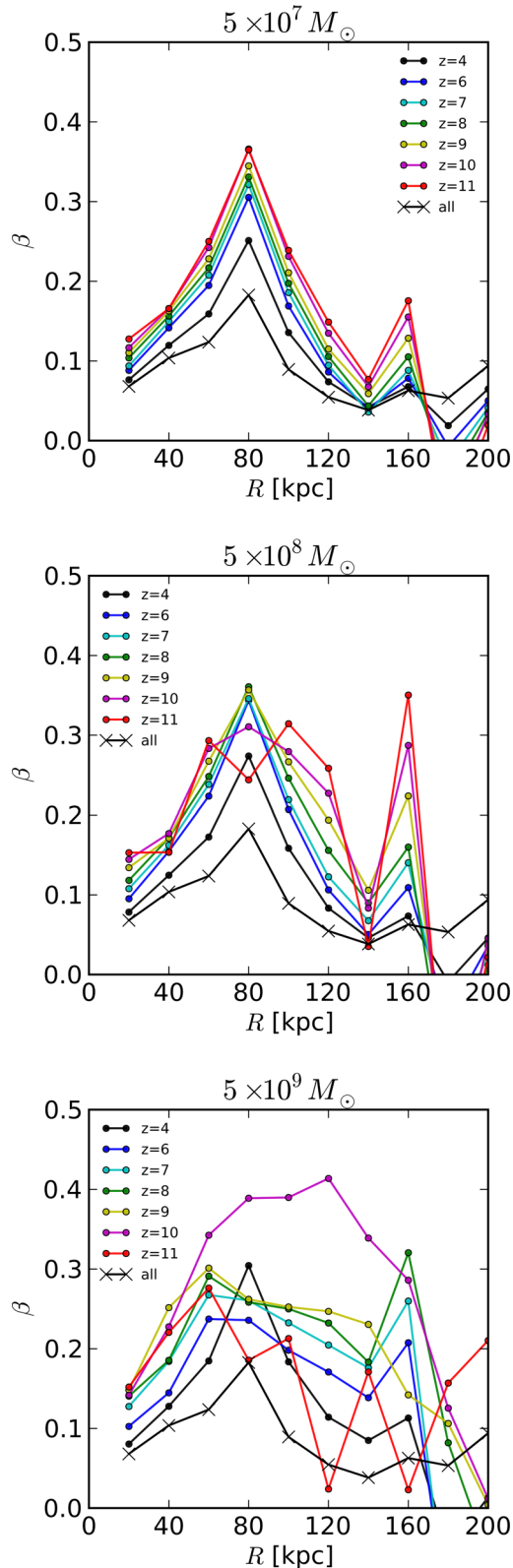


Figure 6. β for various sigma peaks at redshift 0.

$\simeq 4 \times 10^{10}$, respectively. Theoretical work which follows our hypothesis of MPGC formation agrees with our finding of a steep surface density profile of the distribution at $z = 0$ (Moore et al. 2006; Boley et al. 2009; Spitler et al. 2012), whereas the profile of Côté et al. (2001) is designed to follow the gas distribution where data

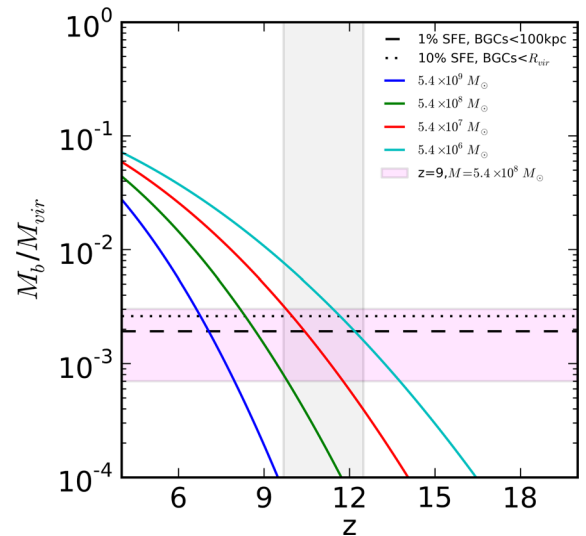


Figure 7. Ability to form the requisite number of stars by the given redshift for an (M, z) cut, assuming instantaneous truncation of reionization. The curves are the conditional mass function for a halo of $3 \times 10^{14} M_\odot$ at $z = 0$. The grey region corresponds to the *WMAP5* measurement for reionization. The magenta region corresponds to the best-fitting model from this work, $z \simeq 9$, $M \simeq 10^8 M_\odot$ with a width equal to the difference in ν between two of our best-fitting models. The black lines correspond to the baryonic mass that is required to produce the present-day BGC population.

are unavailable resulting in a much shallower profile than predicted by our formation theory. Thus, to be consistent with our picture, we regard the integrated mass past 100 kpc as an overestimate when using the profile developed by Côté et al. (2001).

To extend this to a BGC population mass at high redshift, we account for GC destruction which reduces the mass function by a factor of 1.5–4 (Boley et al. 2009). Using a fiducial value of 2, we get an integrated BGC population mass of $\simeq 5.6 \times 10^9$ – $7.6 \times 10^{10} M_\odot$ at high redshift. Finally, in order to compute the total baryonic mass at high redshift, we assume a realistic star formation efficiency in the range of 1–10 per cent.

Assuming a *WMAP5* cosmology, we compute the baryon fraction in collapsed objects for a given dark matter halo minimum mass cutoff by computing the conditional mass function using the Sheth & Tormen (Sheth & Tormen 2002) formalism for a halo of $3 \times 10^{14} M_\odot$ at $z = 0$. Fig. 7 depicts this result. The grey region corresponds to the *WMAP5* measurement for reionization, and the magenta region corresponds to the best-fitting model from this work. We note that the uncertainty of the population mass can be absorbed by the uncertainty in the star formation efficiency, and that a model with the population mass upper bound and 1 per cent star formation efficiency is equivalent to the lower bound and 10 per cent star formation efficiency, and that both are consistent with our best-fitting model of $z \simeq 9$, $M \simeq 10^8 M_\odot$.

We can see that for the mass curves to intersect with the dashed lines of baryonic mass necessary to be generated that $M = 10^9 M_\odot$ is basically ruled out, but for very high redshift of reionization outside of the typical window. We see that lower mass cuts are consistent with lower overdensity peaks (meaning lower redshift as well) and correspond to lower star formation efficiency. Intermediate mass cuts 10^7 – $10^8 M_\odot$ are consistent with higher sigma peaks requiring high star formation efficiency to be consistent with observations. These results provide a consistency check and show that with a realistic star formation efficiency assumption, we can consistently

form the requisite BGCs by the redshift of truncation, which is itself consistent with independent reionization constraints.

4 RESULTING CONSTRAINTS ON REIONIZATION

To summarize the constraints, we performed a linear fit in $(\log(R), \log(\Sigma(R)))$ space on the surface density profile, with slope m , so as to not unduly weight the central points, where error bars come from the variation of that fit over our 100 random lines of sight. This was then compared to the fit to the observational data used by Spitler et al. (2012). For the velocity dispersion profile, we compared the results at 70 kpc to the observational data used by Spitler et al. (2012).

Figs 8 and 9 depict these summary results, respectively, and show that for the line-of-sight velocity dispersion $z \simeq 10$ is the best match for $\simeq 5 \times 10^9 M_\odot$ and $z \simeq 11$ is the best match for $\simeq 5 \times 10^8 M_\odot$ while $\simeq 5 \times 10^7 M_\odot$ points to a cut at much higher redshift outside of our simulation output range. For the surface density profiles, the

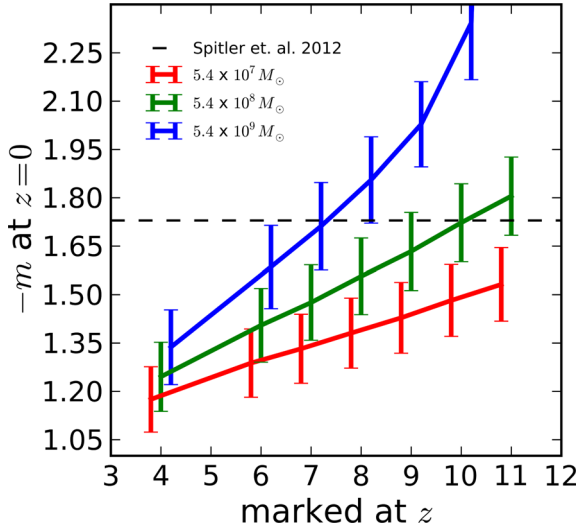


Figure 8. Linear fit in log/log to the density profile at $z = 0$, at each mass threshold marking criterion and marking redshift simulated.

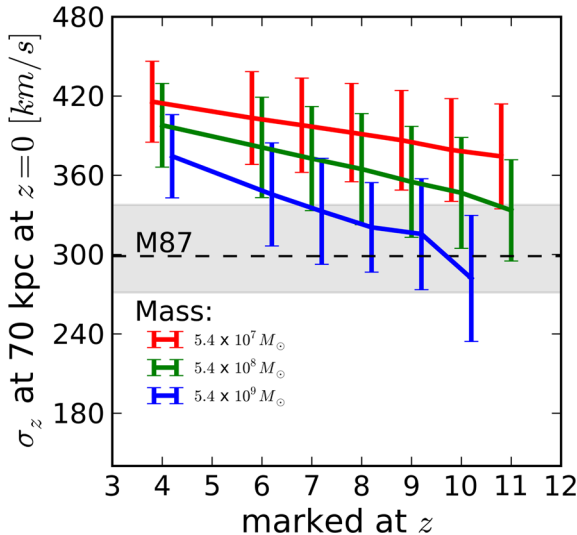


Figure 9. The σ_z value at 70 kpc at each mass threshold marking criterion and marking redshift simulated.

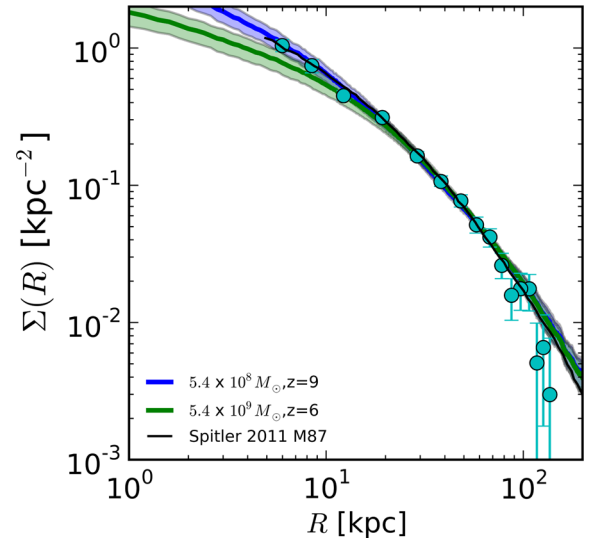


Figure 10. Surface density for $z \simeq 9$, $\simeq 5 \times 10^8 M_\odot$. For reference, we include the model most similar to the best-fitting model of Spitler et al. (2012) $z \simeq 6$, $\simeq 5 \times 10^8 M_\odot$. Both are normalized to the observational value in at 70 kpc. Plotted are the averages over all 100 lines of sight analysed with error bars indicating the dispersion of the average. The black line is the analytic fit arrived on by Spitler et al. (2012), and we see that it fits the observational data equally well as our best-fitting model. Cyan points, with associated error bars, are observational data for M87 MPGCs (Strader et al. 2011).

slope of the linear fit consistently points to the fact that the higher the mass cut, the lower the redshift cut, with similar values of $z \simeq 7$ for $\simeq 5 \times 10^9 M_\odot$, $z \simeq 9 - 10$ for $\simeq 5 \times 10^8 M_\odot$ and $\simeq 5 \times 10^7 M_\odot$ points to much higher than $z \simeq 12$.

As done in Spitler et al. (2012), we are able to put constraints on reionization in a Virgo-like object. We use the Diemand–Moore technique to constrain the rarity of the haloes that MPGCs form within. If the hypothesis that MPGCs formed in high-sigma peaks and that their formation was indeed truncated by reionization is correct our joint constraints from the velocity dispersion, surface density distribution, and star formation efficiency analysis point to a mass of $\sim 5.4 \times 10^8 M_\odot$ ($\simeq 5 \times 10^9 M_\odot$ is ruled out by star formation efficiency analysis, and $\simeq 5 \times 10^7 M_\odot$ ruled out unless reionization completed before $z \simeq 11$). With a mass of $\sim 5.4 \times 10^8 M_\odot$ there is some tension, with the velocity dispersion being a slightly better fit at higher redshift cuts, but with the velocity dispersion not being an especially tight constraint. Thus, we can consistently defer to the more discriminating surface density distribution profile at this mass cut, which clearly points to a value of $z \simeq 9$.

We thus present for our best-fitting model $z \simeq 9$, $M = 5.4 \times 10^8 M_\odot$ the surface density and line-of-sight velocity. Surface density distribution results for the best-fitting model are shown in Fig. 10 and line-of-sight velocity dispersion results for the best-fitting model are shown in Fig. 11. Plotted are the averages over all 100 lines of sight analysed with error bars indicating the dispersion of the average. For reference, we include the model most similar to the best-fitting model of Spitler et al. (2012) $z \simeq 6$, $M = 5.4 \times 10^8 M_\odot$.

5 INTRACLUSTER GLOBULAR CLUSTERS

Simulations of cluster galaxies suggest that between 10 and 50 per cent of stars residing in a cluster are intracluster, that is

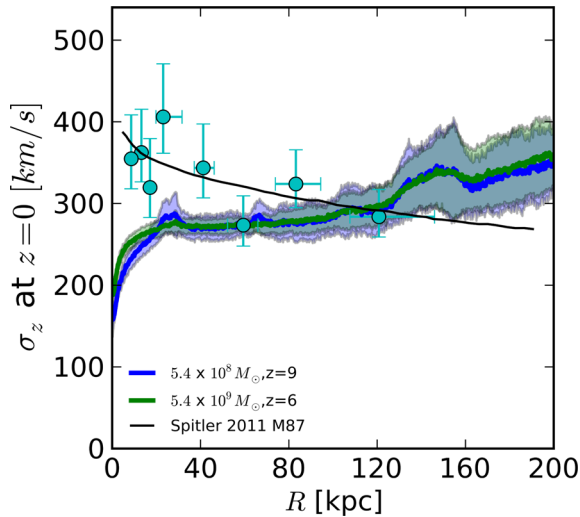


Figure 11. Line-of-sight velocity dispersion for $z \approx 9$, $\approx 5 \times 10^8 M_\odot$. For reference, we include the model most similar the best-fitting model of Spitler et al. (2012) $z \approx 6$, $\approx 5 \times 10^8 M_\odot$. Both are normalized to the observational value in at 70 kpc. Plotted are the averages over all 100 lines of sight analysed with error bars indicating the dispersion of the average. The black line is the analytic fit arrived on by Spitler et al. (2012), we can see that while it correctly accounts for the BCG which our dark matter only simulation does not, and thus is a better fit at inner radii, it performs poorly at greater radii and does not predict the rising velocity dispersion with radius, as we do. Cyan points, with associated error bars, are observational data for M87 MPGCs (Strader et al. 2011).

unattached to any galaxy (Murante et al. 2004; Willman et al. 2004; Sommer-Larsen, Romeo & Portinari 2005; Kravtsov, Vikhlinin & Meshcheryakov 2014), these simulations predict that the intracluster population is older and more centrally concentrated. These can include GCs themselves. Virgo stands out as the nearest system to have a significant intracluster stellar population (Ciardullo et al. 2004).

Intracluster globular clusters (IGCs) are an important probe of the history of galaxies and clusters (West et al. 1995) and can constrain the systems dynamical history. However, obtaining a large sample of these objects is observationally difficult due to their faint nature and the need to pick them out against the background of large galaxies. An observational study of Virgo’s IGCs found four metal-poor IGC candidates (Williams et al. 2007), if this sample is representative of the population as a whole the majority of IGCs are expected to likewise be metal poor, a prediction which was corroborated by Lee, Park & Hwang (2010). Our theoretical work can shed light on this population, and estimate the frequency of IGCs in a Virgo like cluster informing further observational searches seeking to exploit IGCs as cosmological probes.

To identify a population of IGCs, we used the structure and substructure phase-space finder ROCKSTAR (Behroozi, Wechsler & Wu 2013) to identify haloes and subhaloes and within our simulation. ROCKSTAR is a 6D, optionally 7D (temporal), phase-space halo finder which first divides the volume into 3D Friends-of-Friends groups using a large linking length as a parameter. An adaptive phase-space metric is then built so that for each group, 70 per cent of its particles are linked in subgroups, a procedure which is recursively applied. The final step assembles the seed haloes in their densest subgroups assigning each particle to the group closest to it in phase space and performs an unbinding procedure to remove unbound particles.

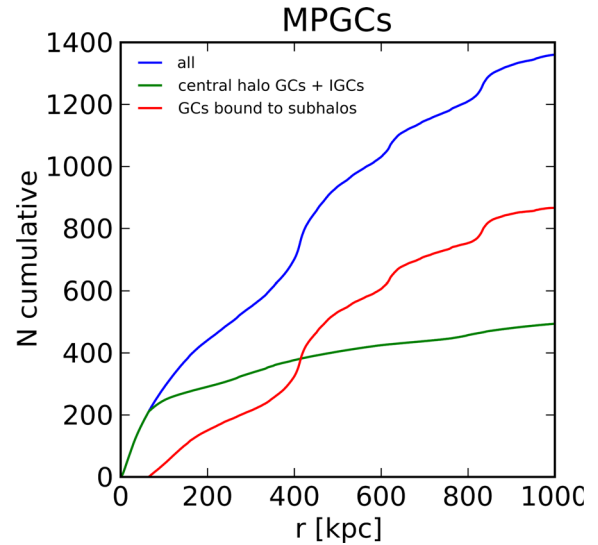


Figure 12. Intracluster globular clusters. Intracluster is defined as not residing within any structure or substructure found by the halo finder ROCKSTAR. In our favoured model within 46 kpc, we have a total mass of $7.2 \times 10^{11} M_\odot$ in particles we identify as tracing the globular cluster distribution. We use the ratio $7.2 \times 10^{11} M_\odot / 161$ as our conversion factor to normalize the number distribution of IGCs we obtain.

We deploy ROCKSTAR in its 6D implementation to form a full halo catalogue at $z = 0$. This catalogue provides positions and radii, among other halo properties, for each halo and subhalo. We use this information to define the intracluster globular cluster population as a subset of the tracer population of our best-fitting model. Particles residing within a halo identified by ROCKSTAR are considered to trace the bound distribution for observational purposes and those which do not are considered to trace the IGC distribution.

To convert this population into an observational estimate, we note that the M87 GC system by Côté et al. (2001) includes data out to 46 kpc and comprises a robust detection of 278 GCs, of which 161 are considered blue metal-poor GCs. In our favoured model within 46 kpc, we have a total mass of $7.2 \times 10^{11} M_\odot$ in particles we identify as tracing the globular cluster distribution. We use the ratio $7.2 \times 10^{11} M_\odot / 161$ as our conversion factor to normalize the number distribution of IGCs we obtain. About 20 per cent of our total GC population is defined as intracluster in our analysis. This is on the same order of the estimate of previous analyses by Yahagi & Bekki (2005), who find that about 30 per cent of all GCs in a rich cluster are intracluster and that IGCs are likely to have a flatter profile, which we likewise see. We can see that the GCs indeed tend to be centrally concentrated around structure as if the analysis were performed for general material a full 43 per cent would be defined as intracluster. The cumulative fraction of IGCs versus radius is given in Fig. 12, we predict ≈ 300 IGCs at the virial radius.

To complete our analysis, we examine bound MPGCs as a function of their v_{\max} noting that this value is for the entire halo, so is in general much higher than that computed for the galaxy alone. We normalize the MPGC distribution such that the largest halo contains 161 MPGCs. We see in Fig. 13 that the number of MPGCs in smaller haloes $v_{\max} < 150$ is negligible compared to both the total number of bound MPGCs and the total number of intracluster MPGCs, and in general a smaller halo of $v_{\max} < 150$ is expected to host < 1 MPGC on average.

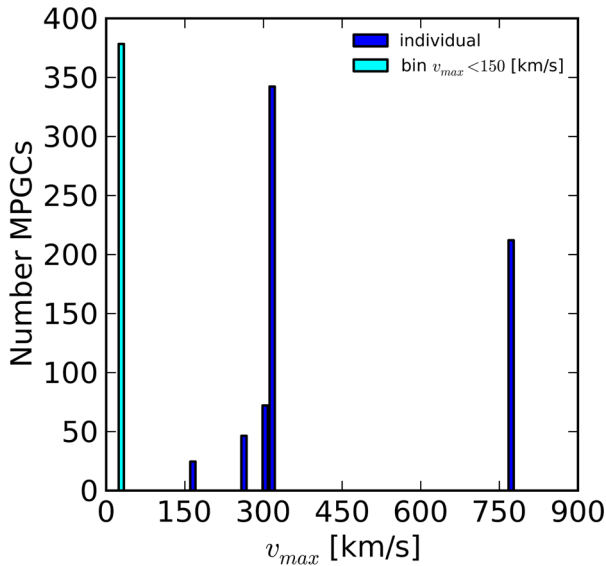


Figure 13. Bound GCs. Bound is defined as residing within any structure or substructure found by the halo finder ROCKSTAR. In our favoured model within 46 kpc, we have a total mass of $7.2 \times 10^{11} M_{\odot}$ in particles we identify as tracing the globular cluster distribution. We use the ratio $7.2 \times 10^{11} M_{\odot}/161$ as our conversion factor to normalize the number distribution of IGCs we obtain.

6 DISCUSSION

We clearly see from the comparison plots that the models are degenerate and both fit the data within the error bars. The best-fitting model therefore must be chosen by incorporating additional information to break this degeneracy, also observed by Moore et al. (2006) and Spitler et al. (2012). We can explain the difference in our conclusion by refinements in the more precise constraints we are able to achieve through a numerical procedure with the relaxed assumption of mass model and spherical symmetry as well as to our choice as to how to address the M, z degeneracy. Specifically, Spitler et al. (2012) use an additional mass threshold based on haloes cooling via atomic cooling only to select star-forming haloes, corresponding to haloes with a virial temperature above $T_{\text{vir}} = 10^4$ K. With a similar assumption, our best-fitting model agrees with Spitler et al. (2012). However, we prefer to relax this assumption, allowing for the possibility of molecular cooling (Tegmark et al. 1997; Abel, Bryan & Norman 2002), and choose to address the M, z degeneracy instead through a star formation efficiency argument in Fig. 7 as done in Boley et al. (2009). Thus, our model differs in its final conclusion precisely due to our relaxed cooling assumption.

We see that the line of sight does indeed have a significant impact on the line-of-sight velocity dispersion observed. Interesting to note is that as the dependence on the surface density depends only logarithmically on line of sight, there is little scatter from the mean in the surface density as seen in summary in Fig. 8, and plotted for one M, z pair in Fig. 10, whereas the line-of-sight velocity dispersion is quite sensitive to the line of sight chosen and can vary by up to $\sim 100 \text{ km s}^{-1}$ in our results as seen in summary in Fig. 9 and plotted for one v in Fig. 11. We see that error bars on these quantities are consistent across redshift and mass pairs.

A point for discussion is in our model there is a tension between the velocity dispersion data and the surface density distribution results, this tension is balanced by our best-fitting model. The surface density distribution results alone point to high-mass intermediate-

redshift formation, or low-mass high-redshift formation sites and epochs, respectively. The velocity dispersion results alone rather point to very large v . Namely, the pairs which produce the flat velocity dispersion curve corresponding to the data and analytic fits of Spitler et al. (2012) correspond to a high redshift and higher mass halo formation sites i.e. very large v . If MPGCs indeed form in such v much larger than our best-fitting results, this would be a hint that the extended in time formation model picture is preferred versus our picture which invokes reionization to truncate GC formation. In this alternative picture preferred by high v results, at low-redshift MPGCs would be required to form in very high mass haloes $\simeq 10^{11}$ and above to maintain the same peak rarity, a conclusion that would be difficult to reconcile with data.

7 CONCLUSIONS

We build upon work by Spitler et al. (2012) identifying MPGCs as forming in high-sigma peaks of the density distribution at high redshift. We propose, validate, and utilize a novel split resolution simulation technique to push resolution to the requisite level to address to confirm the analytic results of Spitler et al. (2012) numerically in an Virgo Cluster analogue. We quantify the dependence of a chosen line of sight for measurements of surface density and velocity dispersion of the globular cluster population finding that surface density measurements to be robust across all lines of sight, the velocity dispersion numerical measurements could have up to an $\sim 100 \text{ km s}^{-1}$ spread. We find the dependence on the chosen line of sight at $z = 0$ of the globular cluster population to be consistent across density peak heights of the initial formation sites. Our results are as follows.

- (i) Our favoured model $z \simeq 9$, $M \simeq 5 \times 10^8 M_{\odot}$ can consistently form the requisite BGCs by $z \simeq 9$, a redshift consistent with reionization constraints.
- (ii) Our best-fitting model relaxes the Spitler et al. (2012) restricted assumptions of an analytic model employing spherical symmetry and atomic cooling only. A redshift of $z \simeq 9$ is more consistent with observational evidence for the reionization window in the cluster environment, versus the much lower $z \simeq 6$ picked out with the Spitler et al. technique.
- (iii) The tension in the velocity dispersion points naturally to further constraints that could come from observations past 130 kpc in M87. We predict a rising velocity dispersion profile. The mass normalization and concentration parameter difference between our simulated cluster and M87 could both shift the velocity dispersion profile upwards, or even potentially influence its slope.
- (iv) We predict $\simeq 300$ intracluster MPGCs in the Virgo cluster. Better observational constraints on the number density of intracluster MPGCs, particularly at high radii, would support or falsify our formation scenario.
- (v) Baryonic physics, realistic globular cluster evaporation modelling, modelling tidal stripping would bring the velocity dispersion simulation results further in line with observations, particularly at the centre of the halo where the BCG resides.

ACKNOWLEDGEMENTS

Simulations were performed on the Monte Rosa system at the Swiss Supercomputing Center (CSCS). CCM was supported by the HP2C programme through the Swiss National Science Foundation. We would like to thank the anonymous referee for their suggestions and comments.

REFERENCES

- Abel T., Bryan G. L., Norman M. L., 2002, *Science*, 295, 93
- Alvarez M. A., Busha M., Abel T., Wechsler R. H., 2009, *ApJ*, 703, L167
- Aubert D., Pichon C., Colombi S., 2004, *MNRAS*, 352, 376
- Beasley M. A., Baugh C. M., Forbes D. A., Sharples R. M., Frenk C. S., 2002, *MNRAS*, 333, 383
- Behroozi P. S., Wechsler R. H., Wu H.-Y., 2013, *ApJ*, 762, 109
- Binney J., Tremaine S., 2011, *Galactic Dynamics*, 2nd edn. Princeton Univ. Press, Princeton, NJ
- Boley A. C., Lake G., Read J., Teyssier R., 2009, *ApJ*, 706, L192
- Brodie J. P., Strader J., 2006, *ARA&A*, 44, 193
- Bromm V., Clarke C. J., 2002, *ApJ*, 566, L1
- Chaboyer B., 1996, *Nucl. Phys. B*, 51, 10
- Ciardullo R., Mihos J. C., Feldmeier J. J., Durrell P. R., Sigurdsson S., 2004, in Duc P.-A., Braine J., Brinks E., eds, *Proc. IAU Symp. 217, The Systematics of Intracluster Starlight*. Astron. Soc. Pac., San Francisco, p. 88
- Côté P. et al., 2001, *ApJ*, 559, 828
- Côté P., West M. J., Marzke R. O., 2002, *ApJ*, 567, 853
- De Angeli F., Piotto G., Cassisi S., Busso G., Recio-Blanco A., Salaris M., Aparicio A., Rosenberg A., 2005, *AJ*, 130, 116
- Diemand J., Madau P., Moore B., 2005, *MNRAS*, 364, 367
- Dotter A. et al., 2009, *ApJ*, 708, 698
- Dressler A., 1979, *ApJ*, 231, 659
- Eisenstein D. J., Hut P., 1998, *ApJ*, 498, 137
- Fan X., Carilli C. L., Keating B., 2006, *ARA&A*, 44, 415
- Fisher D., Illingworth G., Franx M., 1995, *ApJ*, 438, 539
- Forbes D. A., 2006, *Proc. Conference. Globular Clusters: Guides to Galaxies*, 6–10 Mar 2006. Concepcion, Chile
- Geen S., Slyz A., Devriendt J., 2013, *MNRAS*, 429, 633
- Gnedin O. Y., 2009, in de Grijs R., Lepine J., eds, *Proc. IAU Symp. 266, Star Clusters: Basic Galactic Building Blocks Throughout Time and Space*. Cambridge Univ. Press, Cambridge, p. 250
- Gunn J. E., Peterson B. A., 1965, *ApJ*, 142, 1633
- Hahn O., 2008, *RAMSES Tools* (<http://www.exp-astro.phys.ethz.ch/hahn/RamsesTools/>)
- Hanes D. A., Côté P., Bridges T. J., McLaughlin D. E., Geisler D., Harris G. L. H., Hesser J. E., Lee M. G., 2001, *ApJ*, 559, 812
- Hinshaw G. et al., 2013, *ApJS*, 208, 19
- Kravtsov A., Vikhlinin A., Meshcheryakov A., 2014, *ApJ*, preprint (arXiv:1401.7329)
- Lacey C., Cole S., 1994, *MNRAS*, 271, 676
- Larson D. et al., 2011, *ApJS*, 192, 16
- Lee M. G., Park H. S., Hwang H. S., 2010, *Science*, 328, 334
- McLaughlin D. E., 1999, *ApJ*, 512, L9
- Marín-Franch A. et al., 2009, *ApJ*, 694, 1498
- Moore B., Diemand J., Madau P., Zemp M., Stadel J., 2006, *MNRAS*, 368, 563
- Murante G. et al., 2004, *ApJ*, 607, L83
- Muratov A. L., Gnedin O. Y., 2010, *ApJ*, 718, 1266
- Murphy J. D., Gebhardt K., Cradit M., 2014, *ApJ*, 785, 143
- Nagamine K., Ouchi M., Springel V., Hernquist L., 2010, *PASJ*, 62, 1455
- Neilsen E. H., Tsvetanov Z. I., 2009, *ApJ*, 515, L13
- Peebles P. J. E., 1984, *ApJ*, 277, 470
- Peng E. W. et al., 2008, *ApJ*, 681, 197
- Potter D., 2007, *grafic++* (<http://sourceforge.net/projects/grafic/>)
- Press W. H., Schechter P., 1974, *ApJ*, 187, 425
- Rhode K. L., Zepf S. E., Santos M. R., 2005, *ApJ*, 630, L21
- Rosenblatt E. I., Faber S. M., Blumenthal G. R., 1988, *ApJ*, 330, 191
- Santos M. R., 2003, *The High-Redshift Formation of Metal-Poor Globular Cluster Systems*. Springer-Verlag, Berlin
- Scheuer P. A. G., 1965, *Nature*, 207, 963
- Searle L., Zinn R., 1978, *ApJ*, 225, 357
- Sheth R. K., Tormen G., 1999, *MNRAS*, 308, 119
- Sheth R. K., Tormen G., 2002, *MNRAS*, 329, 61
- Sommer-Larsen J., Romeo A. D., Portinari L., 2005, *MNRAS*, 357, 478
- Sparre M., Hansen S. H., 2012, *J. Cosmol. Astropart. Phys.*, 10, 049
- Spitler L. R., Romanowsky A. J., Diemand J., Strader J., Forbes D. A., Moore B., Brodie J. P., 2012, *MNRAS*, 423, 2177
- Strader J. et al., 2011, *ApJS*, 197, 33
- Tegmark M., Silk J., Rees M. J., Blanchard A., Abel T., Palla F., 1997, *ApJ*, 474, 1
- Teyssier R., 2002, *A&A*, 385, 337
- Tweed D., Devriendt J., Blaizot J., Colombi S., Slyz A., 2009, *A&A*, 506, 647
- Tweed D., 2006a, *Projet Horizon – Horizon Project:: HaloMaker* (<http://www.projet-horizon.fr/article283.html>)
- Tweed D., 2006b, *Projet Horizon – Horizon Project:: TreeMaker* (<http://www.projet-horizon.fr/article297.html>)
- Urban O., Werner N., Simionescu A., Allen S. W., Böhringer H., 2011, *MNRAS*, 414, 2101
- West M. J., 1993, *MNRAS*, 265, 755
- West M. J., Côté P., Jones C., Forman W., Marzke R. O., 1995, *ApJ*, 453, L77
- Williams B. F. et al., 2007, *ApJ*, 654, 835
- Willman B., Governato F., Wadsley J., Quinn T., 2004, *MNRAS*, 355, 159
- Yahagi H., Bekki K., 2005, *MNRAS*, 364, L86
- Zinn R., 1985, *ApJ*, 293, 424

APPENDIX A: TECHNICAL DETAILS OF SIMULATION

Using the *RAMSES* code (Teyssier 2002) with initial conditions computed using the Eisenstein & Hut transfer function (Eisenstein & Hut 1998) computed using the *GRAFIC++* code (Potter 2007) we performed a suite of dark matter only zoom cosmological simulations in a Λ CDM cosmology using with cosmological parameters set using *WMAP5* results as listed in Table A1.

The zoom technique selects a subregion of the computational domain to achieve the requisite resolution. To select this subregion, which we desire to form a halo of Virgo-like mass by $z = 0$, we first performed a low-resolution simulation and identify dark matter haloes and subhalos using the *AdaptaHOP* algorithm (Aubert, Pichon & Colombi 2004) in conjunction with a merger tree identification algorithm, as specified in Tweed et al. (2009) as part of the *GaICS* pipeline as *HALOMAKER* (Tweed 2006b) and *TREEMAKER*, respectively (Tweed 2006a). Using the structure identify form a catalogue of dark matter haloes at each simulation output redshift and selected a subsample of haloes with a mass of $1\text{--}3 \times 10^{14} M_{\odot}$, of the order the observed Virgo cluster mass at $z = 0$. To select our best Virgo candidate, we examined assembly history using the merger trees and selected the halo that had a relatively quiescent merger history. We can consider our selected halo relaxed as its last major merger occurs at $z \sim 1.5$. The virial mass of our selected halo, which we define as $M_{200\rho_c}$ is $1.31 \times 10^{14} M_{\odot}$ and the virial radius of our selected halo which we likewise define as $r_{200\rho_c}$ is 1.06 Mpc. This halo was then re-simulated in a zoom simulation focusing the computational resources in the region in which it forms.

Table A1. Cosmological parameters for our simulations.

H_0 [km s ⁻¹ Mpc ⁻¹]	σ_8	n_s	Ω_{Λ}	Ω_m	Ω_b
70.4	0.809	0.809	0.728	0.272	–

This paper has been typeset from a \LaTeX file prepared by the author.